

Review

Au Tip-Enhanced Raman Spectroscopy for Catalysis

Jingang Wang ¹ , Wenhua Qiao ¹ and Xijiao Mu ^{2,*}

¹ College of Sciences, Liaoning Shihua University, Fushun 113001, China; Jingang_wang@lnpu.edu.cn (J.W.); qiao5500hua@163.com (W.Q.)

² School of Mathematics and Physics, Beijing Key Laboratory for Magneto-Photoelectrical Composite and Interface Science, University of Science and Technology Beijing, Beijing 100083, China

* Correspondence: shumuxijiao@163.com; Tel.: +86-180-4003-6755

Received: 30 September 2018; Accepted: 20 October 2018; Published: 23 October 2018



Abstract: Plasmon-driven chemical reactions have been a prospective field for surface plasmon resonance and tip-enhanced Raman scattering. In this review, the principles of tip-enhanced Raman spectroscopy (TERS) are first introduced. Following this, the use of Au TERS for plasmon-driven synthesis catalysis is introduced. Finally, the use of Au TERS for catalysis of dissociation reactions is discussed. This review can provide a deeper understanding of Au TERS for plasmon-driven catalysis.

Keywords: localized surface plasmon resonance (LSPR); surface enhanced Raman scattering (SERS); tip-enhanced Raman spectroscopy (TERS); plasmon-driven surface catalytic reaction

1. Introduction of Tip-Enhanced Raman Spectroscopy (TERS)

Based on local surface plasmon resonance (LSPR), surface-enhanced Raman scattering (SERS) has been investigated intensively and widely applied since 1974 [1–4]. The electric field enhancement of Raman signals can reach 10^8 – 10^{11} [5–7], while chemical enhancement can only reach 10^2 – 10^3 [8–10]. SERS provides an opportunity to overcome the limitation of low Raman scattering cross-sections, and has been widely applied to the investigation of vibration and chemical properties of molecules. However, SERS can only detect the average of all the vibrations of randomly adsorbed molecules on account of its poor spatial resolution [11–14]. Currently, surface plasmons have participated widely in plasmon-driven surface catalytic reactions [2,15–23].

To improve the spatial resolution and overcome the limitation of substrates, the use of tip-enhanced Raman spectroscopy (TERS) emerged in 1985, combining the advantages of SERS and scanning probe microscopy (SPM) techniques [24]. The first TERS results were reported independently by Zenobi, Kawata, Anderson and Pettinger in 2000 [25–27]. Since these first reports, TERS has attracted wide interest as a high-sensitivity optical analytical technique [28,29]. TERS can achieve high spatial resolution beyond the diffraction limit of light and can provide chemical information without sacrificing the molecular resolution at very low temperatures [30]. The electromagnetic enhancement factor of Raman signals at the tip apex in TERS can reach 10^6 . With this significant enhancement, the spatial resolution can be enhanced immensely with a sharp metal tip. The enhancement factor can still be maintained for detection of a single molecule (atomic-scale resolution of 1–10 nm) [31–34].

Another remarkable advance of TERS is that the IR-active and Raman-active modes of target molecules can be obtained simultaneously, whereas SERS can only provide information on the Raman-active modes. The distance between the tip and substrate can be controlled effectively by adjusting the tunneling currents and the ratio between the signal intensities of the Raman-active and IR-active modes can also be controlled. In summary, several unique advantages make TERS a promising technique for investigating samples with weak scattering [35,36].

Samples can be easily contaminated when exposed to air, which can produce an unexpected influence on the results [37–39]. As a result, it can be difficult to distinguish whether the Raman signal

originates from the target molecule, contamination or decomposition of the samples. SPM allows investigations to be monitored in a vacuum, air or aqueous environments. Hence, an ultrahigh vacuum and low temperature environment is usually adopted to enhance the accuracy of TERS results, as these results can shift as a result of the differences in the local environment.

This review focuses on the principles and application of TERS. The fundamental theory and setup of TERS will be presented in detail and current advanced reports on TERS, especially for plasmon-driven reactions, will be presented. SERS and TERS are of great advantage to the field of plasmon-driven surface catalytic reactions. Finally, some challenges and the outlook for the future will be discussed.

2. Brief History of TERS

Normal optical microscopy can only achieve a resolution of 200 nm in the visible region owing to limitations caused by optical diffraction, which can be expressed by Abbe's equation as follows:

$$\Delta x = 0.61\lambda/NA \quad (1)$$

Another disadvantage of optical microscopy is that only an average signal from the target molecules can be obtained. Hence, extensive investigations have been performed to improve spatial resolution through the use of techniques such as scanning near-field optical microscopy (SNOM) with a small aperture [40] and scanning tunneling microscopy (STM) with a narrow tip [41]. By combining these technologies [7,42], four groups are dedicated to developing the spatial resolution of TERS [25–28].

To make the best use of TERS, it is crucial to develop a method that can easily focus the incident laser on the apex of the tips while simultaneously maintaining the intensity and sensitivity of the signal. As shown in Figure 1, TERS is based on SPM technologies such as STM, atomic force microscopy (AFM), shear force microscopy (SFM) and scanning near-field optical microscopy (SNOM).

Using a sharp metal tip (approximately 10–50 nm) and when the focused laser illuminates the apex of the metal or metal-coated tip, a 'hot spot' can be excited in the vicinity of the tip apex due to LSPR [37,43]. Furthermore, as shown in Figure 1a, the intensities of the Raman signals can be enormously enhanced. The most prominent advantage of TERS compared to SERS is the position of the hot spot and the fact that the signal enhancement factor can be effectively controlled by moving the tip and monitoring the distance between the tip and substrate through a feedback system.

As previously introduced, SERS usually requires rough metal surfaces or aggregations of metal nanoparticles to create the hot spot. This roughness is difficult to control and will ultimately lead to randomness in the experimental results. TERS can overcome one of the most severe restrictions in the application of SERS by providing higher accuracy. The spatial resolution of TERS can reach a few nanometers [44,45], even down to the sub-molecular level [46].

With the STM technology shown in Figure 1b, the spatial resolution can reach an atomic level of 0.1 nm and the distance between the tip and substrate can be accurately manipulated by adjusting the tunneling current and sensitive feedback system. The marriage between STM and a ultrahigh vacuum can improve the performance of TERS. However, this type of TERS system is limited by the need for conductive substrates and thin samples.

AFM and SFM are also suitable for use with TERS, as shown in Figure 1c,d [47]. With AFM measurements [48], the samples are not limited and a surface roughness on the micrometer level is acceptable [49]. AFM-TERS can be applied in aqueous environments and may become a suitable technique for biological investigations [35,50–53]. However, the spatial resolution is one nanometer and the tip must be coated with a noble metal, which can easily break during measurements. It should be noted that a dielectric coating on the tip can prevent contamination from the environment or target species, but the coating decreases the plasmonic enhancement. The coating is limited to the nanometer scale (1–2 nm) and must be pinhole-free.

For the SFM-TERS shown in Figure 1d, a metal tip is attached to a high-quality tuning fork as an ultrasensitive feedback system [54,55]. The resulting device is suitable for investigations in aqueous environments as with AFM [56,57], however, more stable tips for SFM are made of metal rather than coated [58,59]. On the other hand, the resolution of SFM is limited by the tuning fork [58,60]. The SNOM shown in Figure 1e is designed to investigate evanescent waves on a surface and includes two types of feedback systems. These are: Constant force (AFM) and shear force (SFM). The resolution of SNOM is strongly dependent on the size of the detector aperture rather than the laser.

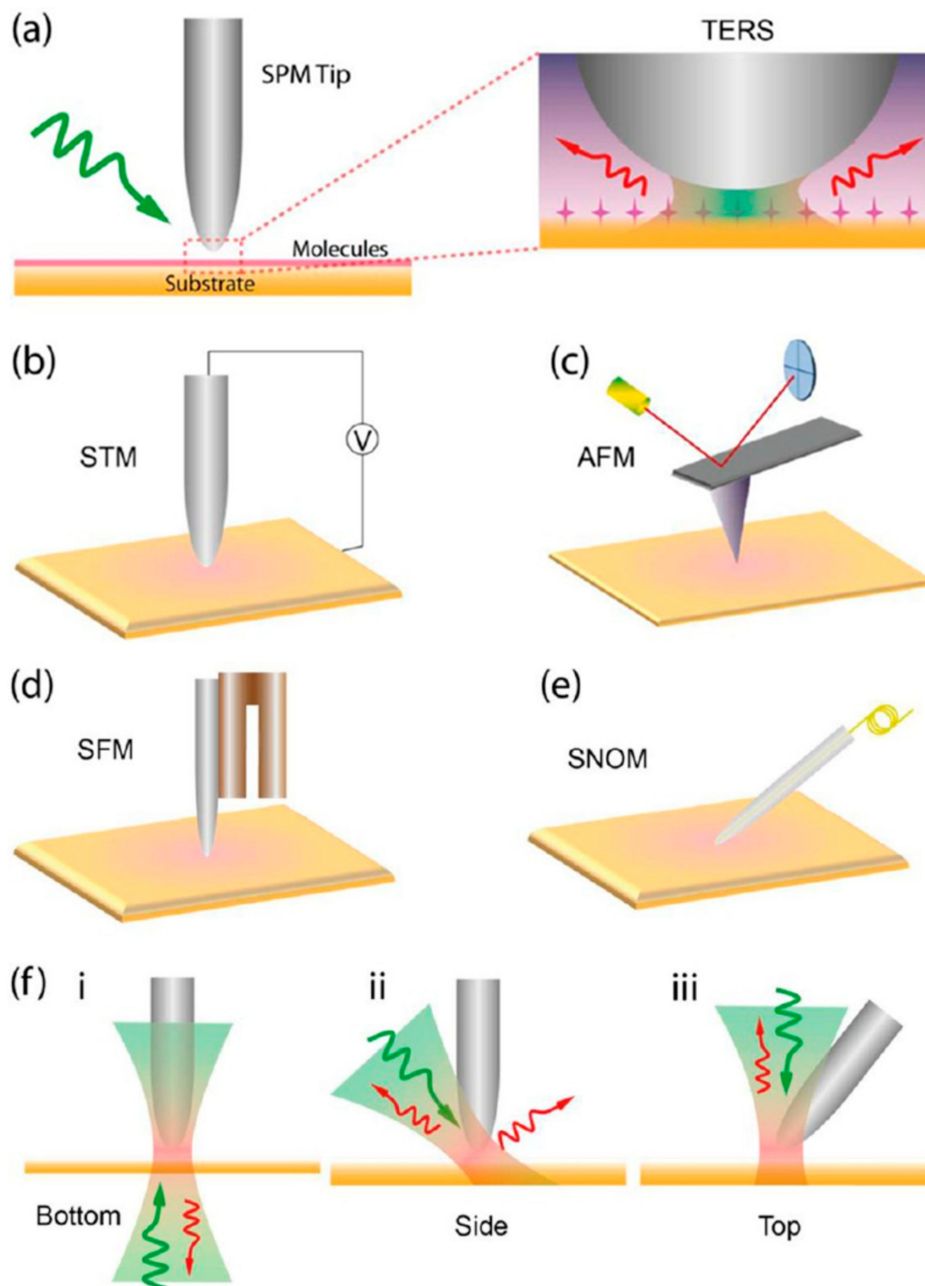


Figure 1. (a) Diagram of TERS, and corresponding SPM technology as (b) STM (c) AFM (d) SFM and (e) SNOM. (f) Three different kinds of excitation and collection: (i) Side excitation and side collection, (ii) bottom excitation and bottom collection and (iii) top excitation and top collection [61].

The electric field enhancement of TERS can be estimated by the following:

$$g = E_{\text{Tip}}/E_0 \quad (2)$$

where E_0 and E_{Tip} are the incident electric field intensity and the enhanced electric field under the tip, respectively. The light intensity of the enhancement is strongly dependent on both the Raman scattering light intensity and the incident laser. Thus, the TERS enhancement factor can be written as follows:

$$EF_{TERS_EM} = g_{Laser}^2 \times g_{Raman}^2 \quad (3)$$

The electric field enhancement is dependent on the frequency and the wavelengths of the Raman scattering light while the illuminating laser differs slightly. When the Raman shift is small, the Raman scattering is almost the same as the electric field enhancement from the laser. In this case, EF_{TERS} can be written as follows:

$$EF_{TERS_EM} = g_{Laser}^2 \times g_{Raman}^2 \approx g^4 \quad (4)$$

Note that the electric field enhancement is very sensitive to the excitation wavelength and the tip material, shape, curvature and radius.

3. Au TERS for Plasmon-Driven Synthesis Catalysis

As previously mentioned, TERS is a promising candidate for investigating the internal mechanism and concepts of plasmon-driven surface catalytic reactions owing to its high sensitivity and spatial resolution [14,17,21]. Additionally, application in high vacuum environments can improve its potential for ultrasensitive spectral analyses on nanoscales. In addition to the enhanced intensity of the Raman signals, the IR-active modes and Fermi resonance can also be simultaneously obtained with high vacuum TERS (HV-TERS). Moreover, the enhancement factor can be modified by adjusting the gap distance.

Here, the selective reduction of 2,4-DNBT to 2,2'-DA-DMAB is used as an example to interpret the unique advantages of HV-TERS over SERS. Based on prior studies, it is revealed that different molecular positions (two nitro groups in different positions) can generate different chemical reactions.

Assisted by surface plasmons (SPs), 2,4-DNBT underwent two different types of reductions, one nitro group of 2,4-DNBT was reduced to an amine, while the other group was reduced to an N=N bond as shown in Figure 2. Figure 2a shows the normal Raman scattering spectrum (NRS) of the 2,4-DNBT powder. Combined with the experimental and theoretical Raman spectra given in Ref [62], it can be determined that the peaks at 1306 cm^{-1} and 1336 cm^{-1} correspond to the NO_2 stretching modes of the two nitro groups, while the peak at 1524 cm^{-1} is attributed to the simultaneous vibration of the nitro groups. Based on the SERS spectrum for 2,4-DNBT (Figure 2b), the disappearance of these Raman peaks related to nitro groups clearly indicates the existence of a surface catalytic reaction. Several new Raman peaks are strongly enhanced and the Raman peak at 1432 cm^{-1} is attributed to the N=N bond. However, the dynamics of the process are hard to determine. The TERS spectrum in Figure 2c differs significantly from the NRS and SERS of 2,4-DNBT.

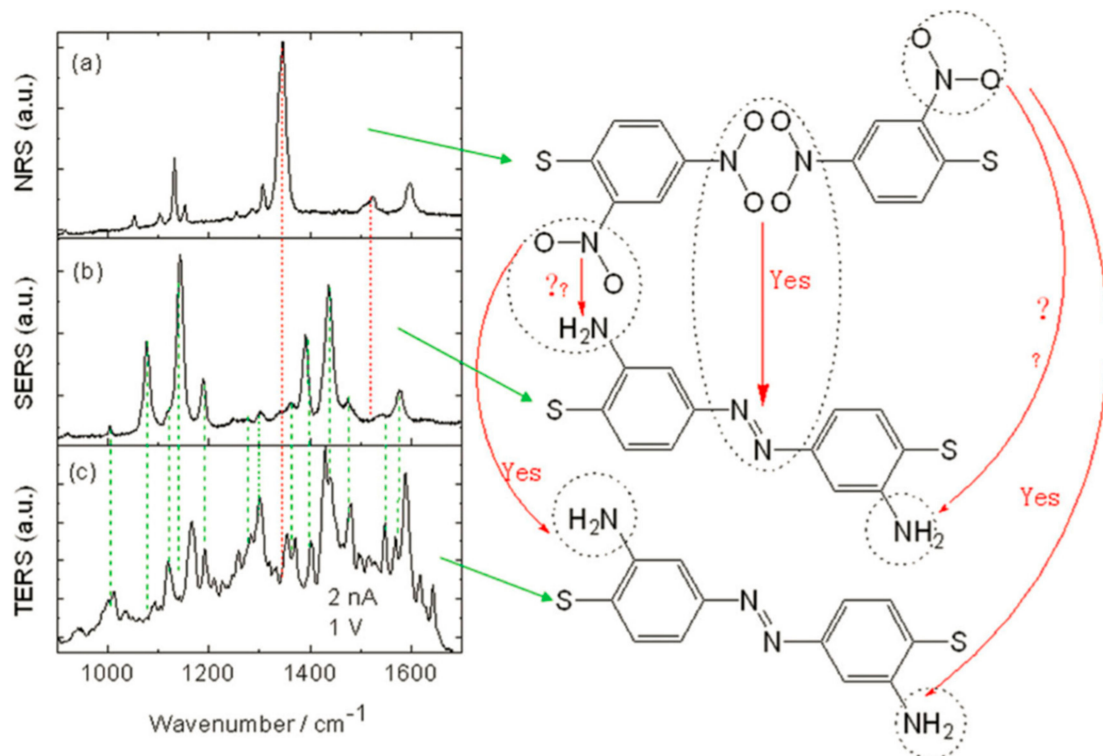


Figure 2. (a) Normal Raman scattering (NRS) of 2,4-DNBT power, (b) and (c) SERS and TER spectra of 2,4-DNBT [62].

In HV-TERS, the IR-active modes of the target molecule can be obtained simultaneously owing to the large electric field gradient effect [63–66]. The Hamiltonian can be expressed as follows [67]:

$$H = H_0 + H_1 + H_2 = \left(\alpha_{\alpha\beta} E_\beta + \frac{1}{3} A_{\alpha,\beta\gamma} \frac{\partial E_{\beta\gamma}}{\partial r} \right) E_\alpha + \frac{1}{3} \left(A_{\gamma,\alpha\beta} E_\gamma + C_{\alpha\beta,\gamma\delta} \frac{\partial E_{\gamma\delta}}{\partial r} \right) \frac{\partial E_{\alpha\beta}}{\partial r} \quad (5)$$

where E_α represents the external electric field and $\frac{\partial E_{\alpha\beta}}{\partial r}$ is the external electric field gradient [67–69].

According to the calculation above, the reason the IR-active modes were obtained in TERS and not in SERS was due to their different types of measurement. TERS is a near-field measurement, in which the electric field gradient effect plays a crucial role. To analyze the electric field gradient effect, calculations based on the TERS system were extensively investigated (Figure 3a). The distribution in Figure 3b shows that the radius with the strongest electric field intensity is approximately 3.0 nm. Figure 3c shows that the strongest intensity is focused in the area of $1.0 \text{ nm} < r < 4.0 \text{ nm}$. Figure 3d shows the ratio of the electric field gradient to the electric field along the tip axis, which is only 1/50.

Figure 3e shows the electric field intensity at the center along the substrate, which differs from Figure 3b where the strongest electric field intensity is focused in the region of $1.0 \text{ nm} < r < 4.0 \text{ nm}$ with the electric field intensity along the tip excluded. The electric field gradient along the substrate in Figure 3f is similar to that along the tip.

According to the ratio in Figure 3g, the effective region is $1.0 \text{ nm} < r < 4.0 \text{ nm}$, and the ratio can increase to 1.2 when the larger terms in Equation (1) are taken into account. Figure 3h shows the distance-dependent ratio of $\frac{\partial E_{\beta\gamma}}{\partial r} / E_\beta$. When the measurement distance is greater than 5 nm in Figure 3h, the effect of the electric field gradient can be almost neglected, and thus the SERS spectra measured in the far field cannot observe the IR-active modes. Based on Figure 3, the reason for the difference between SERS and TERS in Figure 2 can be revealed.

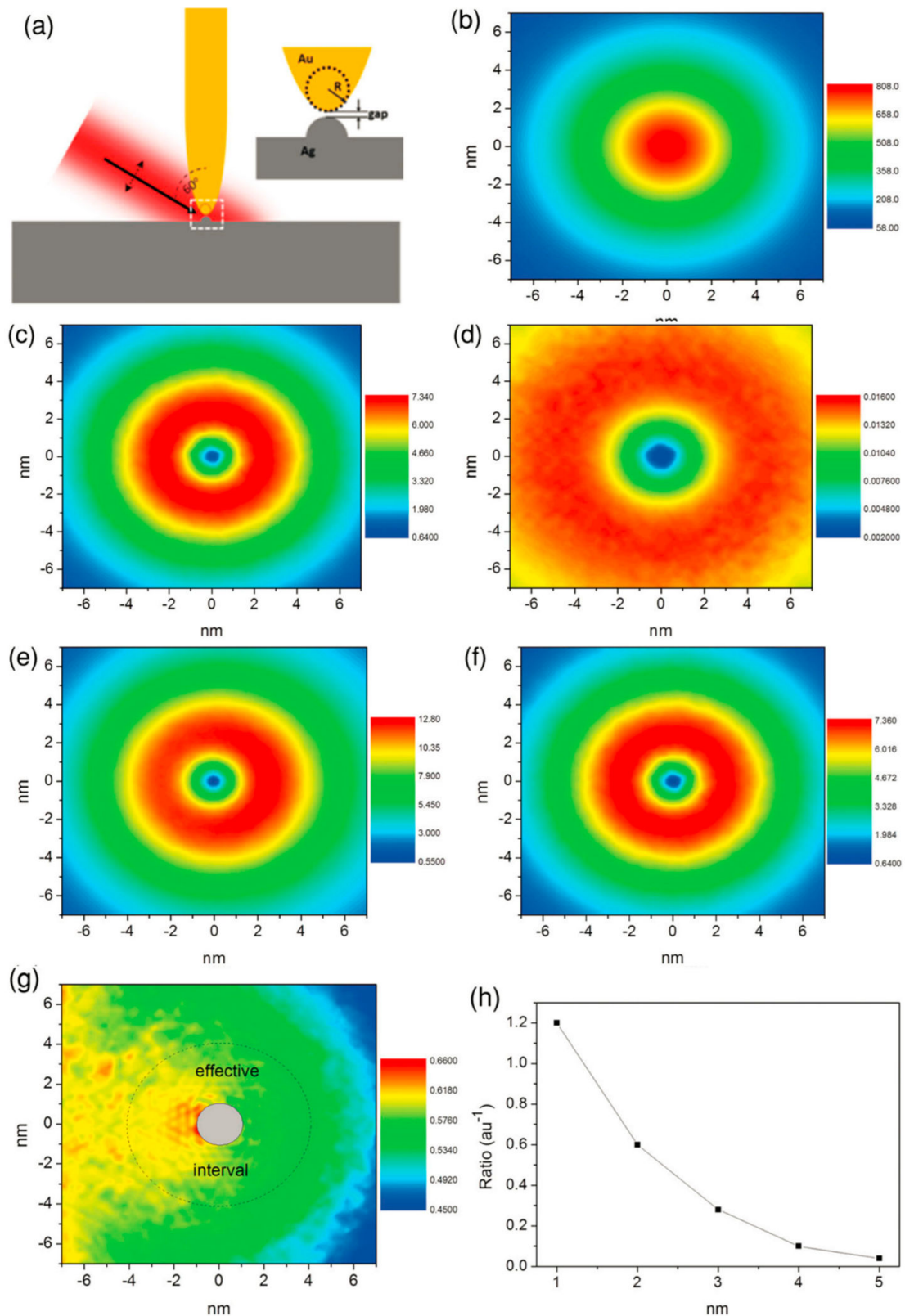


Figure 3. (a) The diagram of TERS system, (b) the simulated electric field intensity at the center, (c) the simulated electric field gradient intensity along tip axis (d) the ratio between electric field gradient and electric field intensity, (e) the simulated electric field intensity along the substrate, (f) the simulated electric field gradient intensity along the substrate, (g) the ratio between electric field gradient and electric field and (h) the distance dependent ratio [62].

Comparing the TERS for 2,4-DNBT in Figure 4a with calculations for 2,2'-DA-DMAB (Figure 4b,c) reveals that the peaks in the TERS spectrum can be approximately assigned to the Raman-active and IR-active modes. Moreover, the 'mysterious' peaks at 1354 cm^{-1} and 1370 cm^{-1} in the TERS spectrum can be effectively interpreted with the Fermi resonance (FR). Further analysis is provided in the supporting information Reference [62]. In summary, TERS can be considered a powerful analytical method for observing Raman and IR spectra at the same time with stronger intensities and better peak classification.

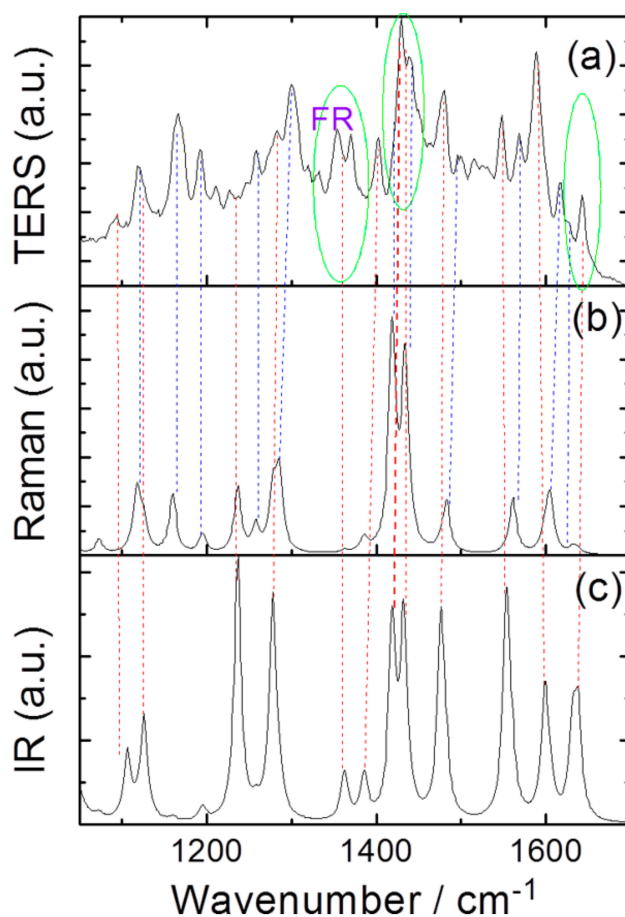


Figure 4. (a) HV-TERS of DMAB, (b) calculated Raman spectrum and (c) calculated IR spectra [62].

According to Figure 5, the ratio between the intensities of the IR-active and Raman-active peaks can be controlled by adjusting the tunneling current. The tunneling current determines the gap distance, i.e., the ratio can be controlled by the gap. When the gap distance decreases, the near-field gradient effect becomes stronger, leading to an increased ratio. In contrast, when the gap is sufficiently large, the IR-active peaks cannot be detected, similar to the SERS shown in Figure 3h. This conclusion is powerful evidence for the interpretation of the disappearance of IR-active modes in SERS.

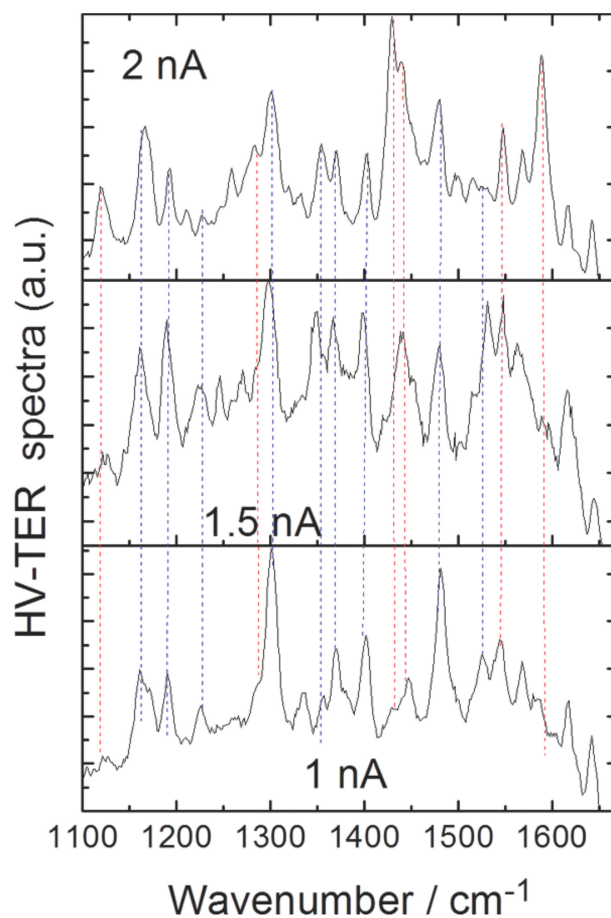


Figure 5. HV-TERS spectra of 2,2'DA-DMAB produced from 2,4-DNBT with different tunneling currents [62].

In previous SERS experiments, dimerization of p-aminothiophenol (PATP) to DMAB was an ideal candidate for revealing plasmon-driven catalytic reactions [16,70–76]. Both theoretical simulations and experimental observations have been investigated in detail, while the dynamic process of the dimerization needs further investigation [77–80]. Based on the TERS, the IR-active modes can be simultaneously obtained and can provide more convincing evidence [69,81–83].

The TERS measurements for PATP on an Au film at different bias voltages in Figure 6 showed that the product was stable and there was little influence on the polarity of the bias voltage, indicating that the product should be structurally symmetric. Moreover, it is obvious that TERS can provide more information than SERS as more Raman peaks appear. Based on previous studies, DMAB can be generated from PATP on Au NPs, while the SERS for PATP on an Au film is similar to the NRS for PATP [71]. The difference in the probabilities for the chemical reaction on different substrates occurs because the plasmonic enhancement on bare Au film is weak.

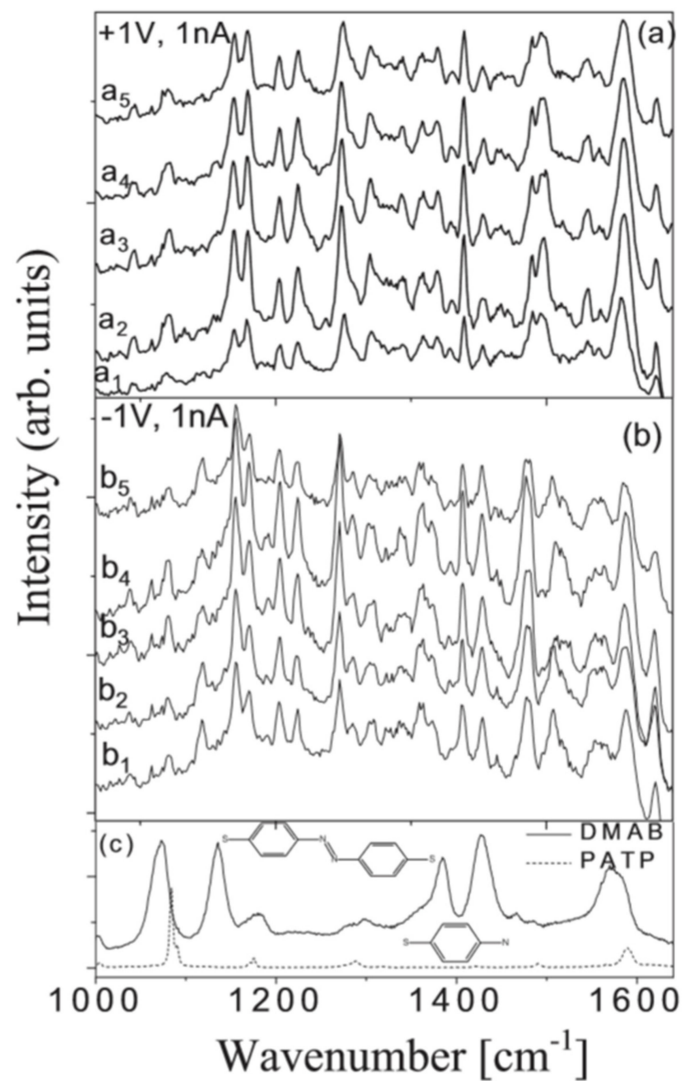


Figure 6. HV-TERS of PATP measured under 1 nA current and (a) +1 V, and (b) −1 V bias voltage at different positions, (c) SERS spectrum of DMAB in Au sol and NRS of PATP [68].

Comparing the experimental TERS spectrum with calculated Raman and IR spectra in Figure 7 shows that all of the peaks can be assigned and the IR-active modes are activated, owing to the electric field gradient effect (molecular quadrupole transitions).

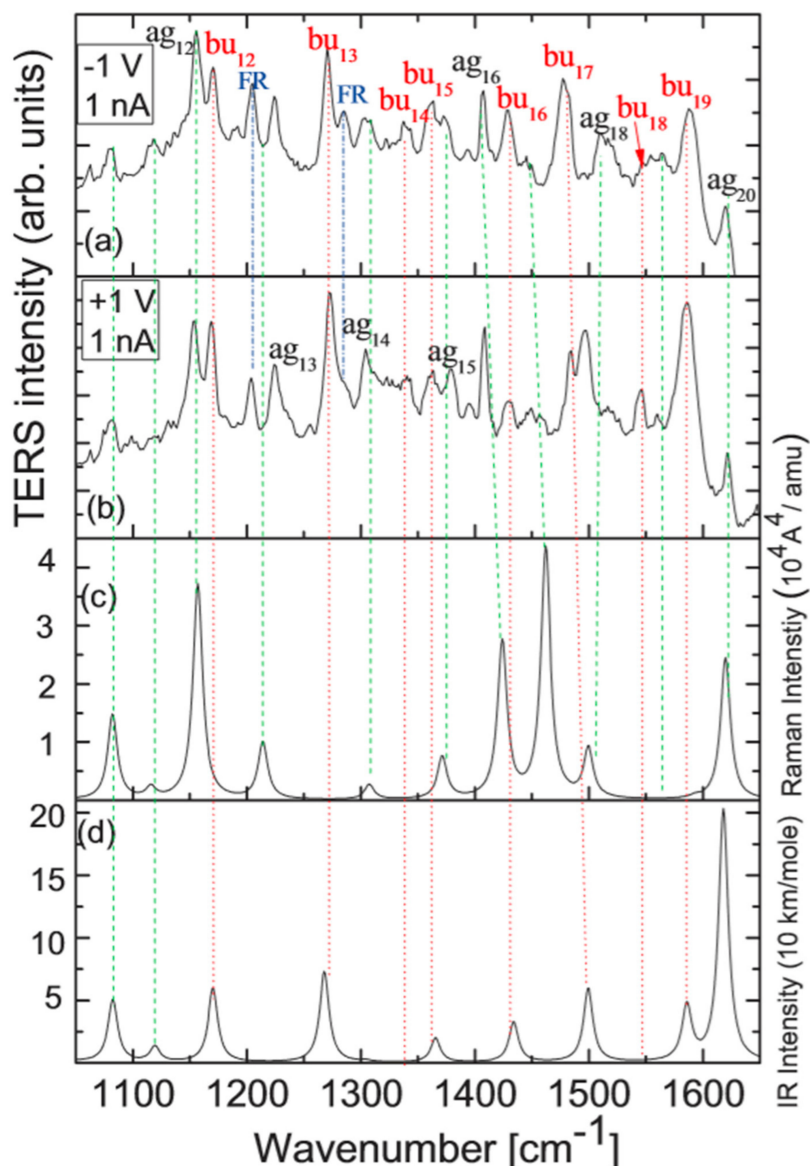


Figure 7. HV-TERS of DMAB that measured under 1 nA current and (a) -1 V and (b) $+1$ V bias voltage, (c) calculated Raman and (d) IR spectra of DMAB [68].

4. Au TERS for Plasmon-Driven Dissociative Catalysis

Plasmon-driven surface catalytic reactions can be detected and analyzed in detail using HV-TERS. Moreover, TERS is able to control the dissociation of target molecules by monitoring the pH value of the environment, which is significant for the environment and investigations of dynamic processes [84–86].

Taking DMAB as the target molecule, experiments and calculations have shown that the N=N bond of DMAB can be selectively broke by hot electrons, see Figure 8. After dissociation, PATP is generated in acidic environments, while 4NBT is generated in alkaline environments. To be more specific, plasmonic hot electrons are temporarily attached to the potential energy surface (PES) of DMAB to form PES, which is accompanied by a decreased reaction barrier. Similar to plasmon-driven catalytic reactions in other environments, the plasmonic hot electrons not only provide the necessary electrons but also the required energy. After the dissociation of DMAB, the radical fragments attach to oxygen or hydrogen ions in alkaline or acidic environments, respectively.

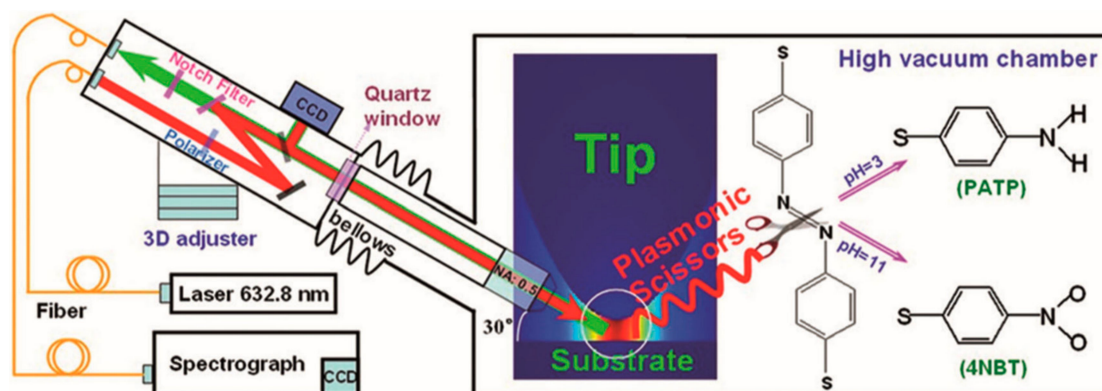


Figure 8. Diagram of plasmonic scissors and the corresponding dynamic process [84].

5. Conclusions

HV-TERS has notable advantages for investigating plasmon-driven reduction and can provide more information with high intensities. The gap can be effectively controlled by adjusting the tunneling current and the degree of surface catalytic reactions can be additionally monitored. The high vacuum environment can prevent contamination and is beneficial for high spatial resolution. The Raman-active and IR-active modes can be observed simultaneously owing to the near-field gradient effect. Based on the experiments and calculated analyses, TERS should be considered a potential technique in the field of ultrasensitive analysis methods.

Author Contributions: Investigation, J.W., X.M.; resources, J.W.; data curation, W.Q.; writing—original draft preparation, J.W.; writing—review and editing, J.W., X.M.; supervision, J.W. and X.M.; project administration, J.W., X.M.; funding acquisition, J.W.

Funding: This work was supported by the National Nature Science Foundation of China (Grant No. 91436102, 11374353, 11474141), Fundamental Research Funds for the Central Universities and talent scientific research fund of LSHU (No. 6008).

Conflicts of Interest: The authors declare no conflicts of interest.

References

1. Fleischmann, M.; Hendra, P.J.; McQuillan, A.J. Raman Spectra of Pyridine Adsorbed at a silver electrode. *Chem. Phys. Lett.* **1974**, *26*, 163–166. [[CrossRef](#)]
2. Sun, M.; Xu, H. A novel application of plasmonics: Plasmon-driven surface-catalyzed reactions. *Small* **2012**, *8*, 2777–2786. [[CrossRef](#)] [[PubMed](#)]
3. Zhang, Z.; Xu, P.; Yang, X.; Liang, W.; Sun, M. Surface plasmon-driven photocatalysis in ambient, aqueous and high-vacuum monitored by SERS and TERS. *J. Photochem. Photobiol. C Photochem. Rev.* **2016**, *27*, 100–112. [[CrossRef](#)]
4. Wang, J.; Feng, N.; Sun, Y.; Mu, X. Nanoplasmon-Semiconductor Hybrid for Interface Catalysis. *Catalysts* **2018**, *8*, 429. [[CrossRef](#)]
5. Lin, W.; Cao, Y.; Wang, P.; Sun, M. Unified Treatment for Plasmon–Exciton Co-driven Reduction and Oxidation Reactions. *Langmuir* **2017**, *33*, 12102–12107. [[CrossRef](#)] [[PubMed](#)]
6. Metiu, H.; Das, P. The Electromagnetic Theory of Surface Enhanced Spectroscopy. *Annu. Rev. Phys. Chem.* **1984**, *35*, 507–536. [[CrossRef](#)]
7. Moskovits, M. Surface-enhanced spectroscopy. *Rev. Mod. Phys.* **1985**, *57*, 783–826. [[CrossRef](#)]
8. Xia, L.; Chen, M.; Zhao, X.; Zhang, Z.; Xia, J.; Xu, H.; Sun, M. Visualized method of chemical enhancement mechanism on SERS and TERS. *J. Raman Spectrosc.* **2014**, *45*, 533–540. [[CrossRef](#)]
9. Otto, A.; Mrozek, I.; Grabhorn, H.; Akemann, W. Surface-enhanced Raman scattering. *J. Phys. Condens. Mat.* **1992**, *4*, 1143–1212. [[CrossRef](#)]
10. Wang, P.; Liu, W.; Lin, W.; Sun, M. Plasmon–exciton co-driven surface catalytic reaction in electrochemical G-SERS. *J. Raman Spectrosc.* **2017**, *48*, 1144–1147. [[CrossRef](#)]

11. Lim, D.K.; Jeon, K.S.; Kim, H.M.; Nam, J.M.; Suh, Y.D. Nanogap-engineerable Raman-active nanodumbbells for single-molecule detection. *Nat. Mater.* **2010**, *9*, 60–67. [[CrossRef](#)] [[PubMed](#)]
12. Sun, M.; Zhang, Z.; Zheng, H.; Xu, H. In-situ plasmon-driven chemical reactions revealed by high vacuum tip-enhanced Raman spectroscopy. *Sci. Rep.* **2012**, *2*, 647. [[CrossRef](#)] [[PubMed](#)]
13. Quan, J.; Cao, E.; Mu, X.; Sun, M. Surface catalytic reaction driven by plasmonic waveguide. *Appl. Mater. Today* **2018**, *11*, 50–56. [[CrossRef](#)]
14. Hartman, T.; Wondergem, C.S.; Kumar, N.; van den Berg, A.; Weckhuysen, B.M. Surface- and Tip-Enhanced Raman Spectroscopy in Catalysis. *J. Phys. Chem. Lett.* **2016**, *7*, 1570–1584. [[CrossRef](#)] [[PubMed](#)]
15. Gao, S.; Ueno, K.; Misawa, H. Plasmonic Antenna Effects on Photochemical Reactions. *Acc. Chem. Res.* **2011**, *44*, 251. [[CrossRef](#)] [[PubMed](#)]
16. Fang, Y.; Li, Y.; Xu, H.; Sun, M. Ascertaining p,p'-dimercaptoazobenzene produced from p-aminothiophenol by selective catalytic coupling reaction on silver nanoparticles. *Langmuir* **2010**, *26*, 7737–7746. [[CrossRef](#)] [[PubMed](#)]
17. Lantman, E.M.; Gaudig, T.D.; Mank, A.J.; Deckert, V.; Weckhuysen, B.M. Catalytic processes monitored at the nanoscale with tip-enhanced Raman spectroscopy. *Nat. Nanotechnol.* **2012**, *7*, 583–586. [[CrossRef](#)] [[PubMed](#)]
18. Christopher, P.; Xin, H.; Linic, S. Visible-light-enhanced catalytic oxidation reactions on plasmonic silver nanostructures. *Nat. Chem.* **2011**, *3*, 467. [[CrossRef](#)] [[PubMed](#)]
19. Zheng, G.; Polavarapu, L.; Liz-Marzán, L.M.; Pastoriza-Santos, I.; Pérez-Juste, J. Gold nanoparticle-loaded filter paper: A recyclable dip-catalyst for real-time reaction monitoring by surface enhanced Raman scattering. *Chem. Commun.* **2015**, *51*, 4572–4575. [[CrossRef](#)] [[PubMed](#)]
20. Linic, S.; Christopher, P.; Xin, H.; Marimuthu, A. Catalytic and Photocatalytic Transformations on Metal Nanoparticles with Targeted Geometric and Plasmonic Properties. *Acc. Chem. Res.* **2013**, *46*, 1890–1899. [[CrossRef](#)] [[PubMed](#)]
21. Zong, H.; Wang, X.; Quan, J.; Tian, C.; Sun, M. Photoinduced charge transfer by one and two-photon absorptions: physical mechanisms and applications. *Phys. Chem. Chem. Phys.* **2018**, *20*, 19720. [[CrossRef](#)] [[PubMed](#)]
22. Xu, P.; Kang, L.; Mack, N.H.; Schanze, K.S.; Han, X.; Wang, H.L. Mechanistic understanding of surface plasmon assisted catalysis on a single particle: Cyclic redox of 4-aminothiophenol. *Sci. Rep.* **2013**, *3*, 2997. [[CrossRef](#)] [[PubMed](#)]
23. Zheng, G.; Kaefer, K.; Mourdikoudis, S.; Polavarapu, L.; Vaz, B.; Cartmell, S.; Bouleghimat, A.; Buurma, N.; Isabel Pastoriza-Santos, L.; Pérez-Juste, J. Palladium nanoparticle-loaded cellulose paper: A highly efficient, robust, and recyclable self-assembled composite catalytic system. *J. Phys. Chem. Lett.* **2014**, *6*, 230–238. [[CrossRef](#)] [[PubMed](#)]
24. Wessel, J. Surface-enhanced optical microscop. *J. Opt. Soc. Am. B* **1985**, *2*, 1538–1541. [[CrossRef](#)]
25. Anderson, M.S. Locally enhanced Raman spectroscopy with an atomic force microscope. *Appl. Phys. Lett.* **2000**, *76*, 3130–3132. [[CrossRef](#)]
26. Hayazawa, N.; Inouye, Y.; Sekkat, Z.; Kawata, S. Metallized tip amplification of near-field Raman scattering. *Opt. Commun.* **2000**, *183*, 333–336. [[CrossRef](#)]
27. Pettinger, B.; Picardi, G.; Schuster, R.; Ertl, G. Surface Enhanced Raman Spectroscopy: Towards Single Molecule Spectroscopy (E). *Electrochemistry* **2000**, *68*, 942–949.
28. Stockle, R.M.; Suh, Y.D.; Deckert, V.; Zenobi, R. Nanoscale chemical analysis by tip-enhanced Raman spectroscopy. *Chem. Phys. Lett.* **2000**, *318*, 131–136. [[CrossRef](#)]
29. Fang, Y.R.; Zhang, Z.L.; Sun, M.T. High vacuum tip-enhanced Raman spectroscopy based on a scanning tunneling microscope. *Rev. Sci. Instrum.* **2016**, *87*, 033104. [[CrossRef](#)] [[PubMed](#)]
30. Jiang, N.; Foley, E.T.; Klingsporn, J.M.; Sonntag, M.D.; Valley, N.A.; Dieringer, J.A.; Seideman, T.; Schatz, G.C.; Hersam, M.C.; Van Duyne, R.P. Observation of Multiple Vibrational Modes in Ultrahigh Vacuum Tip-Enhanced Raman Spectroscopy Combined with Molecular-Resolution Scanning Tunneling Microscopy. *Nano Lett.* **2012**, *12*, 5061–5067. [[CrossRef](#)] [[PubMed](#)]
31. Sonntag, M.D.; Klingsporn, J.M.; Garibay, L.K.; Roberts, J.M.; Dieringer, J.A.; Seideman, T.; Scheidt, K.A.; Jensen, L.; Schatz, G.C.; Van Duyne, R.P. Single-Molecule Tip-Enhanced Raman Spectroscopy. *J. Phys. Chem. C* **2011**, *116*, 478–483. [[CrossRef](#)]
32. Gross, L.; Mohn, F.; Moll, N.; Liljeroth, P.; Meyer, G. The Chemical Structure of a Molecule Resolved by Atomic Force Microscopy. *Science* **2009**, *325*, 1110–1114. [[CrossRef](#)] [[PubMed](#)]

33. Weiss, C.; Wagner, C.; Kleimann, C.; Rohlfing, M.; Tautz, F.S.; Temirov, R. Imaging Pauli repulsion in scanning tunneling microscopy. *Phys. Rev. Lett.* **2010**, *105*, 086103. [[CrossRef](#)] [[PubMed](#)]
34. Steidtner, J.; Pettinger, B. Tip-enhanced Raman spectroscopy and microscopy on single dye molecules with 15 nm resolution. *Phys. Rev. Lett.* **2008**, *100*, 236101. [[CrossRef](#)] [[PubMed](#)]
35. Treffer, R.; Böhme, R.; Deckert-Gaudig, T.; Lau, K.; Tiede, S.; Lin, X.; Deckert, V. Advances in TERS (tip-enhanced Raman scattering) for biochemical applications. *Biochem. Soc. Trans.* **2012**, *40*, 609–614. [[CrossRef](#)] [[PubMed](#)]
36. Yeo, B.-S.; Stadler, J.; Schmid, T.; Zenobi, R.; Zhang, W. Tip-enhanced Raman Spectroscopy—Its status, challenges and future directions. *Chem. Phys. Lett.* **2009**, *472*, 1–13. [[CrossRef](#)]
37. Zhang, W.H.; Cui, X.D.; Yeo, B.S.; Schmid, T.; Hafner, C.; Zenobi, R. Nanoscale Roughness on Metal Surfaces Can Increase Tip-Enhanced Raman Scattering by an Order of Magnitude. *Nano Lett.* **2007**, *7*, 1401–1405. [[CrossRef](#)] [[PubMed](#)]
38. Kudelski, A.; Pettinger, B. SERS on carbon chain segments: Monitoring locally surface chemistry. *Chem. Phys. Lett.* **2000**, *321*, 356–362. [[CrossRef](#)]
39. Etchegoin, P.G.; Lacharmoise, P.D.; Le Ru, E.C. Influence of Photostability on Single-Molecule Surface Enhanced Raman Scattering Enhancement Factors. *Anal. Chem.* **2009**, *81*, 682–688. [[CrossRef](#)] [[PubMed](#)]
40. Wang, J.; Xu, X.; Mu, X.; Ma, F.; Sun, M. Magnetics and spintronics on two-dimensional composite materials of graphene/hexagonal boron nitride. *Mater. Today Phys.* **2017**, *3*, 93–117. [[CrossRef](#)]
41. Pohl, D.W.; Denk, W.; Lanz, M. Optical stethoscopy: Image recording with resolution $\lambda/20$. *Appl. Phys. Lett.* **1984**, *44*, 651–653. [[CrossRef](#)]
42. Pettinger, B.; Schambach, P.; Villagomez, C.J.; Scott, N. Tip-enhanced Raman spectroscopy: Near-fields acting on a few molecules. *Annu. Rev. Phys. Chem.* **2012**, *63*, 379–399. [[CrossRef](#)] [[PubMed](#)]
43. Bailo, E.; Deckert, V. Tip-enhanced Raman scattering. *Chem. Soc. Rev.* **2008**, *37*, 921–930. [[CrossRef](#)] [[PubMed](#)]
44. Chen, C.; Hayazawa, N.; Kawata, S. A 1.7 nm resolution chemical analysis of carbon nanotubes by tip-enhanced Raman imaging in the ambient. *Nat. Commun.* **2014**, *5*, 3312. [[CrossRef](#)] [[PubMed](#)]
45. Wang, J.; Mu, X.; Wang, X.X.; Wang, N.; Ma, F.; Liang, W.; Sun, M. The thermal and thermoelectric properties of in-plane C-BN hybridstructures and graphene/h-BN van der Waals heterostructures. *Mater. Today Phys.* **2018**, *5*, 29–57.
46. Zhang, R.; Zhang, Y.; Dong, Z.C.; Jiang, S.; Zhang, C.; Chen, L.G.; Zhang, L.; Liao, Y.; Aizpurua, J.; Luo, Y.E.; et al. Chemical mapping of a single molecule by plasmon-enhanced Raman scattering. *Nature* **2013**, *498*, 82–86. [[CrossRef](#)] [[PubMed](#)]
47. Ding, Q.; Shi, Y.; Chen, M.; Li, H.; Yang, X.; Qu, Y.; Liang, W.; Sun, M. Ultrafast Dynamics of Plasmon-Exciton Interaction of Ag Nanowire- Graphene Hybrids for Surface Catalytic Reactions. *Sci. Rep.* **2016**, *6*, 32724. [[CrossRef](#)] [[PubMed](#)]
48. Liu, W.; Lin, W.; Zhao, H.; Wang, P.; Sun, M. The nature of plasmon-exciton codriven surface catalytic reaction. *J. Raman Spectrosc.* **2018**, *49*, 383–387. [[CrossRef](#)]
49. Schmid, T.; Yeo, B.-S.; Leong, G.; Stadler, J.; Zenobi, R. Performing tip-enhanced Raman spectroscopy in liquids. *J. Raman Spectrosc.* **2009**, *40*, 1392–1399. [[CrossRef](#)]
50. Kong, L.R.; Mu, X.J.; Fan, X.; Li, R.; Zhang, Y.; Song, P.; Ma, F.; Sun, M. Site-selected N Vacancy of g-C₃N₄ for Photocatalysis and Physical Mechanism. *Appl. Mater. Today* **2018**, *13*, 329–338. [[CrossRef](#)]
51. Pozzi, E.A.; Sonntag, M.D.; Jiang, N.; Klingsporn, J.M.; Hersam, M.C.; Van Duyne, R.P. Tip-Enhanced Raman Imaging: An Emergent Tool for Probing Biology at the Nanoscale. *Acs Nano* **2013**, *7*, 885–888. [[CrossRef](#)] [[PubMed](#)]
52. Wood, B.R.; Bailo, E.; Khiavi, M.A.; Tilley, L.; Deed, S.; Deckert-Gaudig, T.; McNaughton, D.; Deckert, V. Tip-enhanced Raman scattering (TERS) from hemozoin crystals within a sectioned erythrocyte. *Nano Lett.* **2011**, *11*, 1868–1873. [[CrossRef](#)] [[PubMed](#)]
53. Bailo, E.; Deckert, V. Tip-enhanced Raman spectroscopy of single RNA strands: Towards a novel direct-sequencing method. *Angew. Chem. Int. Ed. Engl.* **2008**, *47*, 1658–1661. [[CrossRef](#)] [[PubMed](#)]
54. Li, R.; Zhang, Y.; Xu, X.; Zhou, Y.; Chen, M.; Sun, M. Optical characterizations of two-dimensional materials using nonlinear optical microscopies of CARS, TPEF, and SHG. *Nanophotonics* **2018**, *7*, 873–881. [[CrossRef](#)]
55. Martin, O.J.F.; Girard, C. Controlling and tuning strong optical field gradients at a local probe microscope tip apex. *Appl. Phys. Lett.* **1997**, *70*, 705–707. [[CrossRef](#)]

56. Lin, W.; Xu, X.; Quan, J.; Sun, M. Propagating surface plasmon polaritons for remote excitation surface-enhanced Raman scattering spectroscopy. *Appl. Spectrosc. Rev.* **2018**, *53*, 771–782. [[CrossRef](#)]
57. Leong, J.K.; Williams, C.C. Shear force microscopy with capacitance detection for near-field scanning optical microscopy. *Appl. Phys. Lett.* **1995**, *66*, 1432–1434. [[CrossRef](#)]
58. Rodriguez, R.D.; Sheremet, E.; Müller, S.; Gordan, O.D.; Villabona, A.; Schulze, S.; Hietschold, M.; Zahn, D.R.T. Compact metal probes: A solution for atomic force microscopy based tip-enhanced Raman spectroscopy. *Rev. Sci. Instrum.* **2012**, *83*, 123708. [[CrossRef](#)] [[PubMed](#)]
59. Wang, X.; Cao, E.; Zong, H.; Sun, M. Plasmonic electrons enhanced resonance Raman scattering (EERRS) and electrons enhanced fluorescence (EEF) spectra. *Appl. Mater. Today* **2018**, *13*, 298–302. [[CrossRef](#)]
60. Stadler, J.; Schmid, T.; Zenobi, R. Developments in and practical guidelines for tip-enhanced Raman spectroscopy. *Nanoscale* **2012**, *4*, 1856–1870. [[CrossRef](#)] [[PubMed](#)]
61. Zhang, Z.; Sheng, S.; Wang, R.; Sun, M. Tip-Enhanced Raman Spectroscopy. *Anal. Chem.* **2016**, *88*, 9328–9346. [[CrossRef](#)] [[PubMed](#)]
62. Sun, M.; Zhang, Z.; Chen, L.; Li, Q.; Sheng, S.; Xu, H.; Song, P. Plasmon-Driven Selective Reductions Revealed by Tip-Enhanced Raman Spectroscopy. *Adv. Mater. Interfaces* **2014**, *1*, 1300125. [[CrossRef](#)]
63. Sun, M.; Zhang, Z.; Chen, L.; Sheng, S.; Xu, H. Plasmonic Gradient Effects on High Vacuum Tip-Enhanced Raman Spectroscopy. *Adv. Opt. Mater.* **2014**, *2*, 74–80. [[CrossRef](#)]
64. Sun, M.; Zhang, Z.; Chen, L.; Xu, H. Tip-Enhanced Resonance Couplings Revealed by High Vacuum Tip-Enhanced Raman Spectroscopy. *Adv. Opt. Mater.* **2013**, *1*, 449–455. [[CrossRef](#)]
65. Zhang, Z.; Sun, M.; Ruan, P.; Zheng, H.; Xu, H. Electric field gradient quadrupole Raman modes observed in plasmon-driven catalytic reactions revealed by HV-TERS. *Nanoscale* **2013**, *5*, 4151–4155. [[CrossRef](#)] [[PubMed](#)]
66. Fang, Y.; Zhang, Z.; Chen, L.; Sun, M. Near field plasmonic gradient effects on high vacuum tip-enhanced Raman spectroscopy. *Phys. Chem. Chem. Phys.* **2015**, *17*, 783–794. [[CrossRef](#)] [[PubMed](#)]
67. Buckingham, A.D. Permanent and induced molecular moments and long-range intermolecular forces. *Adv. Chem. Phys.* **1967**, *12*, 107.
68. Sun, M.; Fang, Y.; Zhang, Z.; Xu, H. Activated vibrational modes and Fermi resonance in tip-enhanced Raman spectroscopy. *Phys. Rev. E* **2013**, *87*, 020401. [[CrossRef](#)] [[PubMed](#)]
69. Ayars, E.; Hallen, H.D. Electric Field Gradient Effects in Raman Spectroscopy. *Phys. Rev. Lett.* **2000**, *85*, 4180–4183. [[CrossRef](#)] [[PubMed](#)]
70. Lin, W.; Ren, X.; Cui, L.; Sun, M. Electro-optical tuning of plasmon-driven double reduction interface catalysis. *Appl. Mater. Today* **2018**, *11*, 189–192. [[CrossRef](#)]
71. Huang, Y.; Fang, Y.; Yang, Z.; Sun, M. Can p,p'-Dimercaptoazobisbenzene Be Produced from p-Aminothiophenol by Surface Photochemistry Reaction in the Junctions of a Ag Nanoparticle–Molecule–Ag (or Au) Film? *J. Phys. Chem. C* **2010**, *114*, 18263–18269. [[CrossRef](#)]
72. Yang, X.; Yu, H.; Guo, X.; Ding, Q.; Pullerits, T.; Wang, R.; Zhang, G.; Liang, W.; Sun, M. Plasmon-exciton coupling of monolayer MoS₂-Ag nanoparticles hybrids for surface catalytic reaction. *Mater. Today Energy* **2017**, *5*, 72–78. [[CrossRef](#)]
73. Campion, A.; Kambhampati, P. Surface-enhanced Raman scattering. *Chem. Soc. Rev.* **1998**, *27*, 241–250. [[CrossRef](#)]
74. Cao, E.; Guo, X.; Zhang, L.; Shi, Y.; Lin, W.; Liu, X.; Fang, Y.; Zhou, L.; Sun, Y.; Song, Y. Electrooptical Synergy on Plasmon—Exciton—Cocdriven Surface Reduction Reactions. *Adv. Mater. Interfaces* **2017**, *4*, 1700869. [[CrossRef](#)]
75. Lin, W.; Cao, E.; Zhang, L.; Xu, X.; Song, Y.; Liang, W.; Sun, M. Electrically enhanced hot hole driven oxidation catalysis at the interface of a plasmon-exciton hybrid. *Nanoscale* **2018**, *10*, 5482–5488. [[CrossRef](#)] [[PubMed](#)]
76. Zhou, Q.; Li, X.; Fan, Q.; Zhang, X.; Zheng, J. Charge Transfer between Metal Nanoparticles Interconnected with a Functionalized Molecule Probed by Surface-Enhanced Raman Spectroscopy. *Angew. Chem.* **2006**, *118*, 4074–4077. [[CrossRef](#)]
77. Park, W.H.; Kim, Z.H. Charge transfer enhancement in the SERS of a single molecule. *Nano Lett.* **2010**, *10*, 4040–4048. [[CrossRef](#)] [[PubMed](#)]
78. Zhang, Z.L.; Sheng, S.X.; Wang, R.M.; Sun, M.T. Tip-Enhanced Raman Spectroscopy. *Anal. Chem.* **2016**, *88*, 9328–9346. [[CrossRef](#)] [[PubMed](#)]
79. Sun, M.; Zhang, Z.; Wang, P.; Li, Q.; Ma, F.; Xu, H. Remotely excited Raman optical activity using chiral plasmon propagation in Ag nanowires. *Light Sci. Appl.* **2013**, *2*, e112. [[CrossRef](#)]

80. Ding, Q.; Li, R.; Chen, M.; Sun, M. Ag nanoparticles-TiO₂ film hybrid for plasmon-exciton co-driven surface catalytic reactions. *Appl. Mater. Today* **2017**, *9*, 251–258. [[CrossRef](#)]
81. Moskovits, M.; DiLella, D.P. Intense quadrupole transitions in the spectra of molecules near metal surfaces. *J. Chem. Phys.* **1982**, *77*, 1655–1660. [[CrossRef](#)]
82. Lin, W.; Shi, Y.; Yang, X.; Li, J.; Cao, E.; Xu, X.; Pullerits, T.; Liang, W.; Sun, M. Physical Mechanism on Exciton-Plasmon Coupling Revealed by Femtosecond Pump-Probe Transient Absorption Spectroscopy. *Mater. Today Phys.* **2017**, *3*, 33–40. [[CrossRef](#)]
83. Zong, H.; Wang, J.; Mu, X.; Xu, X.; Li, J.; Wang, X.; Long, F.; Wang, X.; Sun, M. Physical mechanism of photoinduced intermolecular charge transfer enhanced by fluorescence resonance energy transfer. *Phys. Chem. Chem. Phys.* **2018**, *20*, 13558. [[CrossRef](#)] [[PubMed](#)]
84. Sun, M.; Zhang, Z.; Kim, Z.H.; Zheng, H.; Xu, H. Plasmonic scissors for molecular design. *Chem. Eur. J.* **2013**, *19*, 14958–14962. [[CrossRef](#)] [[PubMed](#)]
85. Wang, J.; Lin, W.; Xu, X.; Ma, F.; Sun, M. Plasmon-Exciton Coupling Interaction for Surface Catalytic Reactions. *Chem. Rec.* **2018**, *18*, 481–490. [[CrossRef](#)] [[PubMed](#)]
86. Xu, X.; Shi, Y.; Liu, X.; Sun, M. Femtosecond dynamics of monolayer MoS₂-Ag nanoparticles hybrid probed at 532 nm. *Chem. Phys. Lett.* **2018**, *692*, 208–213. [[CrossRef](#)]



© 2018 by the authors. Licensee MDPI, Basel, Switzerland. This article is an open access article distributed under the terms and conditions of the Creative Commons Attribution (CC BY) license (<http://creativecommons.org/licenses/by/4.0/>).